Addition of bismuth stimulates photocatalysis by UiO-66/TiO2: synergistic effect between Bi3+ and metallic Bi0

Mitra Saffari, Massomeh Ghorbanloo, Ali Morsali, Heba Elmaghrabi, Djamel Bezzerga, Jisang Hong, Tia Maria Howayek, Roland Habchi, Roman Viter, Bernard Fraisse, et al.

To cite this version:

Mitra Saffari, Massomeh Ghorbanloo, Ali Morsali, Heba Elmaghrabi, Djamel Bezzerga, et al.. Addition of bismuth stimulates photocatalysis by UiO-66/TiO2: synergistic effect between Bi3+ and metallic Bi0. Journal of Photochemistry and Photobiology A: Chemistry, 2026, 471, pp.116667. ⟨10.1016/j.jphotochem.2025.116667⟩. ⟨hal-05295840⟩

HAL Id: hal-05295840
https://hal.umontpellier.fr/hal-05295840v1

Submitted on 13 May 2026

Journal of Photochemistry & Photobiology, A: Chemistry 471 (2026) 116667

Contents lists available at ScienceDirect

Journal of Photochemistry & Photobiology, A: Chemistry

journal homepage: www.elsevier.com/locate/jphotochem

Addition of bismuth stimulates photocatalysis by UiO-66/TiO_2: synergistic effect between Bi^{3+} and metallic Bi^0

Mitra Saffari [a], Massomeh Ghorbanloo [a,**], Ali Morsali [b], Heba H. Elmaghrabi [c,d], Djamel Bezzerga [e], Jisang Hong [e], Tia Maria Howayek [c,f], Roland Habchi [f], Roman Viter [g], Bernard Fraisse [h], Igor Iatsunskyi [i], Emerson Coy [i], David Cornu [c], Amr A. Nada [c,j,*], Mikhael Bechelany [c,*]

[a] Chemistry Department, Faculty of Science, University of Zanjan, Zanjan, P. O. Box: 4537138791, Iran
[b] Department of Chemistry, Faculty of Sciences, Tarbiat Modares University, P.O. Box 14155-4838, Tehran, Iran
[c] Institut Européen des Membranes, IEM, UMR 5635, Univ Montpellier, ENSCM, CNRS, Montpellier, France
[d] Department of Refining, Egyptian Petroleum Research Institute, Cairo, Nasr City P.B, 11727, Egypt
[e] Department of Physics, Pukyong National University, Busan 48513, Republic of Korea
[f] EC2M, Faculty of sciences 2, Campus Pierre Gemayel - Fanar, Lebanese University, 90656, Lebanon
[g] Institute of Atomic Physics and Spectroscopy, University of Latvia, 19 Raina Blvd., LV 1586 Riga, Latvia
[h] Institut Charles Gerhardt Montpellier (ICGM) – UMR 5253, University of Montpellier, CNRS, 34090 Montpellier, France
[i] NanoBioMedical Centre, Adam Mickiewicz University, Wszechnicy Piastowskiej 3, 61-614 Poznan, Poland
[j] Material Research and Technology Department, Luxembourg Institute of Science and Technology, 28 Avenue des Hauts-Fourneaux, Esch-Sur-Alzette 4362, Luxembourg

ARTICLE INFO

Keywords:
Bi^0-UiO-66/TiO_2-Bi^3
Electrospinning
Hydrogen evolution
Water splitting
Synergistic effect

ABSTRACT

In this work, innovative Bi^0-UiO-66/TiO_2-Bi^{3+} photocatalysts were synthesized by electrospinning. The morphological and spectroscopic analyses showed the existence of Bi^{3+} and Bi^0 (metallic) and also Zr (in the valence states +IV) on the surface of TiO_2 nanofibers (NFs). The band gap decrease from 3.09 eV in pristine TiO_2 to 2.8 eV in Bi-UiO-66/TiO_2 NFs improved the light-harvesting efficiency. Hydrogen production was tested under visible light irradiation using a 500 W linear halogen lamp (420–600 nm) positioned at 10 cm from the reaction solution. Hydrogen production via photocatalysis was increased by 2-fold and 24-fold with Bi^0-UiO-66/TiO_2-Bi^{3+} (3734 $\mu molg^{-1}$ h^{-1}) compared to UiO-66/TiO_2 and TiO_2 NFs, respectively. This enhancement was attributed to the synergistic effect between Bi^0 and Bi^{3+} (as predicted also by the density functional theory model) and the improved visible light absorption by Bi^0. Additionally, the formation of a Bi_2O_3-TiO_2 heterojunction promoted the separation of photoinduced charge carriers. Lastly, the prepared Bi^0-UiO-66/TiO_2-Bi^{3+} NFs demonstrated high recyclability without photocatalytic activity reduction.

1. Introduction

Hydrogen is considered one of the most promising green alternatives to fossil fuels [1]. Its production by photocatalysis involves the conversion of solar energy into chemical energy [2], and is a critical research area to address the escalating global energy crisis and environmental challenges [3,4]. Various semiconductor photocatalysts, such as TiO_2, ZnO and Fe_2O_3, have been extensively studied for hydrogen production [5,6]. However, the photocatalytic efficiency of semiconductor photocatalysts remains limited due to various challenges, including photocorrosion, low photon absorption efficiency, inefficient charge separation, and limited number of catalytic active sites [2]. TiO_2 displays excellent stability, low cost, environmental friendliness, and suitable band-edge positions for redox reactions, but its photocatalytic activity under visible light is limited due to its wide bandgap (~3.2 eV for anatase).

Therefore, several authors have investigated metal-organic frameworks (MOFs) as photocatalysts. MOFs are crystalline, porous, hybrid materials [7–10] known for their tunable pore structures, high specific surface area with numerous active catalytic sites, and customizable

---

* Corresponding authors at: Institut Européen des Membranes, IEM, UMR 5635, Univ Montpellier, ENSCM, CNRS, Montpellier, France.
** Corresponding author.
E-mail addresses: m_ghorbanloo@znu.ac.ir (M. Ghorbanloo), amr.nada@list.lu (A.A. Nada), mikhael.bechelany@umontpellier.fr (M. Bechelany).

https://doi.org/10.1016/j.jphotochem.2025.116667
Received 11 June 2025; Received in revised form 20 July 2025; Accepted 1 August 2025
Available online 5 August 2025

electronic and optical properties [11]. For instance, zirconium (Zr(IV))-based MOFs, such as UiO-66, exhibit remarkable thermal and chemical stability [12,13], making them promising candidates for photocatalytic applications in water environments [14]. However, the relatively wide band gap energy of UiO-66 (~3.8 eV) results in low photoconversion efficiency, restricting its practical application for solar light harvesting [2,15]. Various strategies have been proposed to enhance the photocatalytic efficiency of UiO-66, including band gap engineering [16] and element doping [17]. Particularly, the formation of heterojunction structures improves the photocatalytic performance of UiO-66 by creating interfaces between semiconductors [18,19]. Integrating TiO_2 with MOFs can establish a localized environment that increases the concentration of composite materials at the surface, addressing the issue of reduced light trapping efficiency caused by the agglomeration of TiO_2 particle. Additionally, the encapsulation of metal nanoparticle (NP) catalysts within the MOF cavity prevents their aggregation, while the interactions between the MOF surface and NPs contribute to the optimization of their catalytic performance [20].

Bismuth (Bi)-based materials present a viable alternative to precious metals in the fabrication of photocatalyst [21]. Bi is an affordable, environmentally friendly, and abundant active metal [22], known for its localized surface plasmon resonance (LSPR) properties [23]. Bi doping enhances the absorption range of TiO_2. Furthermore, as an electron acceptor, Bi helps to reduce electron-hole (e^-/h^+) recombination, thereby boosting the photocatalytic efficiency [24,25].

Therefore, we developed novel Bi^0-UiO-66/TiO_2-Bi^{3+} composite photocatalysts through a simple one-step electrospinning method that facilitated the in-situ formation of metallic Bi. In this study, Bi use (both Bi^{3+} and Bi^0) was limited to small amounts incorporated in the UiO-66/TiO_2 composite. Bi is considered a relatively low-toxic and environmentally compatible element compared with other heavy metals. Moreover, Bi-based materials, including Bi_2O_3 and elemental Bi, are generally stable and not prone to significant leaching in typical photocatalytic conditions. Therefore, the risk of Bi leaching and its environmental impact are minimal, in line with the principles of safe and sustainable material use. The structure and physicochemical properties of the resulting NFs were thoroughly characterized and their photocatalytic performance for water splitting under visible light was assessed. Bi^0-UiO-66/TiO_2-Bi^{3+} demonstrated outstanding hydrogen generation efficiency compared to UiO-66/TiO_2 and TiO_2, primarily due to the synergistic effect between Bi^{3+} and metallic Bi^0. Additionally, the electronic density of states (DOS) of all composites was computed and density functional theory (DFT) was employed to model the complete band alignment scheme of the Bi-UiO-66/TiO_2 system.

2. Experimental

2.1. Materials

All materials used in this study are listed in Table 1.

Table 1
Materials, purity, and supplier.

Material	Purity	Supplier
$Zr(NO_3)_2.3H_2O$	99.99 %	Sigma Aldrich
$Bi(NO_3)_3.5H_2O$	99.99 %	Sigma Aldrich
1,4-benzenedicarboxylic acid	98 %	Sigma Aldrich
Titanium tetraisopropoxide	97 %	Sigma Aldrich
Polyvinylpyrrolidone (PVP)	$M_w = 1{,}300{,}000$ g/Mol	Sigma Aldrich
Acetic acid	98 %	Sigma Aldrich
Absolute ethanol	99 %	Sigma Aldrich
Absolute methanol	99 %	Sigma Aldrich
N,N-dimethylformamide	99.8 %	Sigma Aldrich
Nafion perfluorinated Resin solution		Sigma Aldrich

2.2. Preparation of Bi-UiO-66/TiO_2 composite NFs

Zirconium chloride (58.4 mg, 0.25 mmol), 1,4-benzenedicarboxylic acid (BDC) (41.5 mg, 0.25 mmol) and *N,N*-dimethylformamide (DMF) (22 g, 300 mmol) were used for UiO-66 fabrication following the protocol in [26]. Then, UiO-66 (0.124 g, 0.15 mmol) and $Bi(NO_3)_3$ (0.6 mol %, 0.9 mol%, and 1.2 mol%) were dissolved in ethanol (2 mL) and DMF (0.5 mL) by stirring for 30 min, and were added to the precursor solution (prepared by stirring 0.3 g PVP with titanium tetraisopropoxide in 3 mL ethanol and 2 mL acetic acid at room temperature for 30 min). After 60 min, electrospinning was performed using a syringe with a stainless-steel needle (0.7 mm in diameter), flow rate of 1 mL/h, chamber temperature of 38 ± 5 °C, 1.25 kV/cm, and a rotating coil (400 rpm) covered with aluminum foil. NFs were heat-treated at 400 °C (ramp rate = 5 °C/min in air) for 4 h.

2.3. Sample characterization

Samples were analyzed with standard procedures as previously described: X-ray diffraction (XRD) [27], scanning electron microscopy (SEM) and transmission electron microscopy (TEM) [28], energy-dispersive X-ray spectroscopy (EDX) [28], Raman microscopy, Fourier transform infrared (FT–IR) spectrophotometry, ultraviolet-visible (UV–Vis) spectrophotometry and photoluminescence analysis [29], and X-ray photoelectron spectroscopy (XPS) [30]. Quantifications were performed from the peak area of the high-resolution XPS spectra after correction with suitable sensitivity factors and background signal correction with the Shirley method [31]. The atom concentrations at the samples surface were determined as described in [32]. All core levels binding energies were relative to the C—C bonds in the C1s spectrum at 284.8 eV.

2.4. Photocatalytic H_2 generation

H_2 production was carried out and monitored as described in [29,33].

2.5. Computational methods

The lattice parameters derived from the experimental results, a DFT approach that relies on the parameterization designed for solids using the PBEsol approximation [34,35], and plane-wave pseudopotentials in Quantum ESPRESSO [36] were employed to predict the electronic DOS. The kinetic energy and charge density cut-off values were 60 Ry and 480 Ry. A Monkhorst-Pack grid of 10 × 10 × 10 k-points was used for all samples, except for UiO-66, where only the zone center (Γ point) was used due to the large cell parameters. The core-valence state interactions were described using ultrasoft pseudopotentials [35]. For Bi and O_2, fifteen ($5d^{10}\ 6s^2\ 4p^3$) and six valence electrons ($2s^2\ 2p^4$), respectively, were considered. The Hubbard correction method (PBU + U) was employed to accurately determine the energy band gap [36,37]. The Hubbard U parameter was 8 eV for the Ti 3d and Zr 4d states. The spin-orbit coupling for α-Bi_2O_3 was not calculated because it required excessive computing power due to the lower α-Bi_2O_3 symmetry and larger number of atoms in the UiO-66 unit cell.

3. Results and discussion

In the present study, $Bi(NO_3)_3$ and UiO-66 MOFs were introduced in the TiO_2 structure to enhance H_2 production by photocatalytic water splitting. The obtained samples (pristine TiO_2, UiO-66 before and after calcination, UiO-66-TiO_2, 0.6 %Bi-UiO-66/TiO_2, 0.9 %Bi-UiO-66/TiO_2 and 1.2 %Bi-UiO-66/TiO_2) were characterized before utilization for H_2 production.

3.1. Characterization of the prepared samples

The XRD patterns of anatase TiO_2 (JCPDS No. 01–084-1285) were observed in all samples (Fig. 1) [38]. Moreover, a broad XRD peak at 2θ = 30.8^0 in the Bi-UiO-66/TiO_2 NFs corresponded to the (121) diffraction plane of brookite (JCPDS No. 29–1360) [39]. The absence of distinct peaks for Bi_2O_3 and UiO-66 indicated that these components were either finely dispersed or too small to be identified by XRD. The stability of UiO-66 after calcination was established in previous studies that used thermogravimetric analysis [26,40] and was further confirmed by the FT-IR and XPS results presented below. The distinct and narrow diffraction peaks observed in UiO-66 after heat treatment indicated successful crystallization. However, the broadening of these peaks with increasing Bi_2O_3 concentrations suggested a decrease in the crystallinity and crystallite size of anatase TiO_2. The unit cell volume of pristine TiO_2 and 1.2 %Bi-UiO-66/TiO_2 increased from 136.52 Å^3 to 136.85 Å^3 (as determined by Rietveld refinement of the XRD data), likely due to Ti^{4+} replacement by Bi^{3+} ions on the surface of the TiO_2 crystallites. Indeed, Bi^{3+} ions have a larger ionic radius than Ti^{4+} ions [(r (Ti^{4+}) = 60.5 pm, r (Bi^{3+}) = 103 pm], and both are 6-fold coordinated [41]. Conversely, the crystallite size decreased from 24.2 nm in pristine TiO_2 to 15.2 nm in 1.2 %Bi-UiO-66/TiO_2. The increased ionic radius of Bi^{3+} may lead to modifications in the anatase crystal structure, potentially hindering the growth of crystallites [50]. Our earlier studies [27,29,30] showed that larger ions (e.g., Ce^{3+} and Cs^{1+}) cannot enter the TiO_2 lattice. However, they can replace Ti^{4+} ions on the surface of TiO_2 crystallites, thereby restricting the anatase phase growth. This is achieved by reducing the interactions between the crystallites and the rearrangement of lattice Ti and O atoms. As a result, the formation of Bi-O-Ti bonds on the TiO_2 crystallite surface contributes to limit crystallite interactions and restricts the rearrangement of Ti and O atoms in the lattice. This, in turn, hinders the development of anatase phase crystallinity, leading to a reduction in the crystallite size of Bi_2O_3-containing TiO_2 NFs. Based on the Rietveld refinement results, strain was higher in 1.2 %Bi-UiO-66/TiO_2 than in pristine TiO_2 (84 % versus 39 %), likely due to the lattice distortion and crystallite size reduction. Brookite phases (JCPDS No. 20–1960) were detected in small quantities in Bi-UiO-66-TiO_2 NFs. As the Bi content increased, the peaks slightly broadened and the crystallite size decreased, suggesting minor distortions in the crystal structure [42].

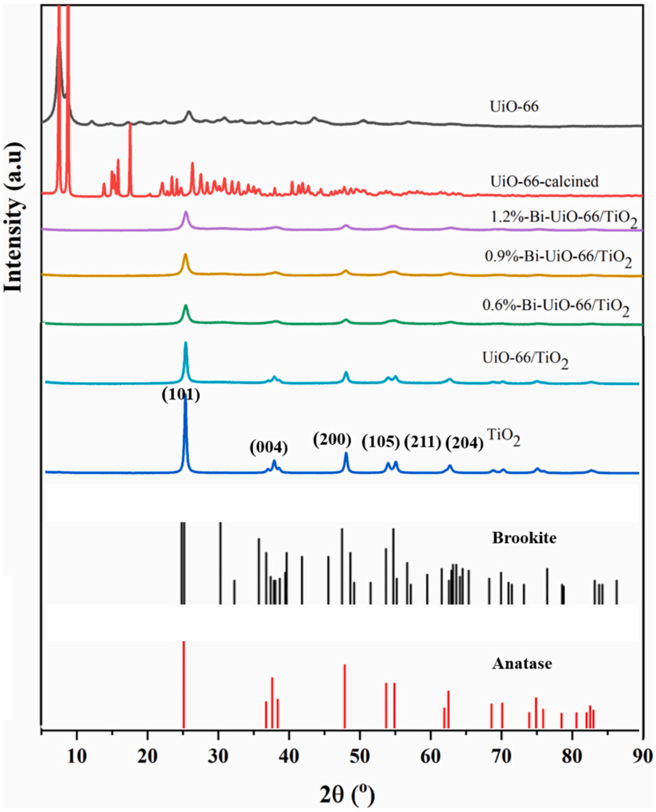

Fig. 1. XRD patterns of the indicated samples. The peaks at 2θ = 25.07^0, 37.8^0, 48.1^0, 53.9^0, 55.2^0 are linked to the (101), (004), (200), (105), (211) and (204) lattice planes of anatase TiO_2, respectively.

The XPS analysis of UiO-66 revealed three peaks (532.2, 531.1, and 529.8 eV) in the O 1s spectrum (Fig. 2a) that correspond to surface-adsorbed hydroxyl groups, C═O, and Zr—O bonds, respectively [43]. The slight shift in O 1s binding energy observed in calcined UiO-66 could be attributed to the evaporation of the trapped solvent (DMF) within the MOF network. In the case of 1.2 %Bi-UiO-66/TiO_2, the three peaks in the O 1s spectrum (529.6, 530.1, and 531.70 eV) were assigned to Zr—O and Ti—O, to Bi^{3+}-O, and to O—H bonds in water adsorbed on the surface, respectively [44].

The XPS analysis of TiO_2 physicochemical interactions revealed two peaks in the Ti 2p spectrum at 458.60 eV ($2p_{3/2}$) and 464.44 eV ($2p_{1/2}$) (Fig. 2b) [45]. In the 1.2 %Bi-UiO-66 sample, these peaks shifted to higher binding energies (464.64 and 458.8 eV), indicating the presence of Bi^{3+} on TiO_2 surface. This shift can be attributed to the lower Pauling electronegativity of Ti (1.5 versus 2.02 for Bi). This causes charge transfers from Ti^{4+} to Bi^{3+} through Ti-O-Bi bonding, thereby reducing the electron density around Ti atoms. This finding confirmed the interaction between Bi^{3+} and TiO_2. In the 1.2 %Bi-UiO-66-TiO_2 sample, the Ti $2p_{3/2}$ and Ti $2p_{1/2}$ spin–orbit splitting values of 6.3 eV suggests that Ti^{4+} was the dominant oxidation state [27].

Upon deconvolution, the XPS spectra of UiO-66 and heat-treated UiO-66 showed two peaks at 184.6 (Zr $3d_{3/2}$) and 182.7 eV (Zr $3d_{5/2}$) (Fig. 2c), indicating that Zr^{4+} interacts with BDC [46]. This suggests that the Zr chemical environment remained unchanged and that UiO-66 maintained its stability during the heat treatment (~400 °C). Zr^{4+} presence was confirmed by the binding energy difference between these peaks. In the case of 1.2 %Bi-UiO-66/TiO_2, the binding energies of Zr $3d_{5/2}$ and Zr $3d_{3/2}$ shifted slightly to 184.5 and 182.3 eV, respectively. This indicates that the incorporation of Bi NP into the UiO-66/TiO_2 matrix enhances the electron density of Zr clusters. It also supports the hypothesis that electrons are transferred from Bi NPs to the MOF, promoting the interaction between Bi NPs and UiO-66, and enhancing the photocatalytic activity [47]. The possibility of electrostatic interactions between Bi NPs and UiO-66 is supported also by the fact that the ζ potential of Bi NPs is negative [48] and that of UiO-66 is positive [49]. Bi NPs were not detected by XRD in the composite sample (Fig. 2b), but only by high-resolution TEM.

After deconvolution, the C 1s spectrum of UiO-66 displayed three peaks that correspond to C—C (284.6 eV), C-O/C-N (286.3 eV) and O-C=O (288.6 eV) and are associated with terephthalic acid (Fig. 2d). In calcined UiO-66, the intensity of the peak at 286.3 eV decreased, indicating the near-complete removal of DMF from UiO-66 surface [50].

The 1.2 %Bi-UiO-66-TiO_2 sample (Fig. 2e) exhibited peaks at 164.8 eV and 159.2 eV that corresponded to Bi^{3+} $4f_{5/2}$ and $4f_{7/2}$, respectively. The binding energy difference (~5.5 eV) between these peaks confirmed that the valence state of the Bi species in 1.2 %Bi-UiO-66/TiO_2 was +3. This confirmed the successful incorporation of Bi into the NF structure and its potential role in enhancing photocatalytic activity [51,52]. As previously mentioned, the charge transfers from Ti^{4+} to Bi^{3+} ions via Ti-O-Bi bonds result in a higher electron density around Bi ions and lower electron density around Ti ions. This explains the XPS peak shift to higher binding energies for Ti ions and to lower binding energies for Bi ions, compared with pure Bi_2O_3. This shift indicates interactions between Ti and Bi species in the NFs, suggesting that their interplay alters their electronic structures [53]. Moreover, the two peaks at 162.8 and 157.5 eV were attributed to the Bi^0 $4f_{5/2}$ and $4f_{7/2}$ states [23]. Wu et al., suggested that the formation of Bi^0 species in samples remains uncertain and that during calcination, Bi^{3+} may be partially reduced to Bi^0 due to the presence of carbonaceous species [25]. The binding energy of Bi $4f_{7/}$

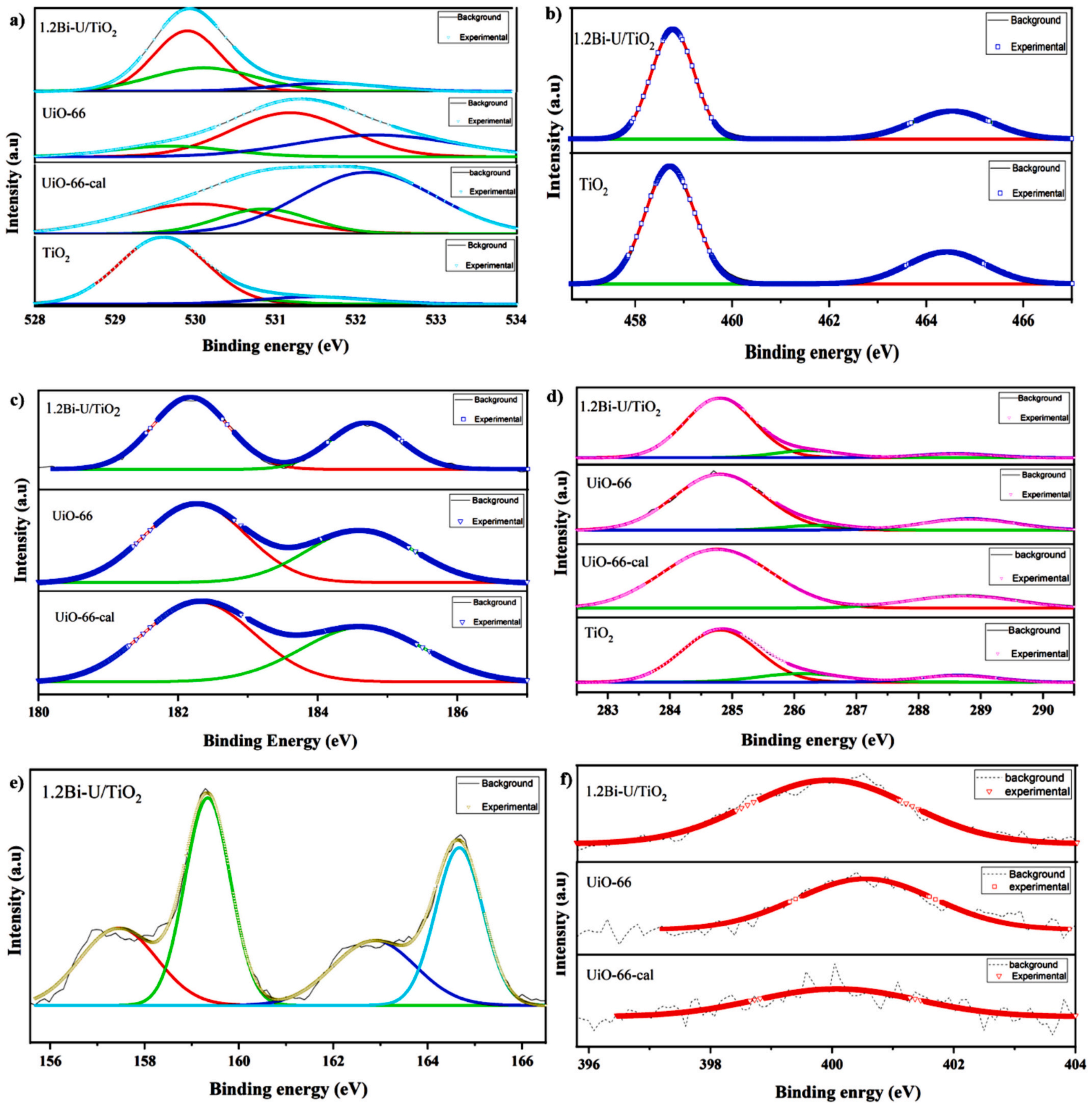

Fig. 2. High-resolution XPS spectra of O 1s (a), Ti 2p (b), Zr 2p (c), C 1s (d), Bi 4f (e) and N 1s (f) for the indicated samples. Solid lines, experimental results; dashed lines, fitted curves after background removal.

$_2$ in the 1.2 %Bi-UiO-66/TiO$_2$ composite was higher than that of pure metallic Bi^0 [53,54]. This suggests that in the composite, the electronic interactions of Bi^0 species might be altered compared with pure metallic Bi. This change may affect their properties and reactivity within the composite structure. As previously discussed, the charge transfer from Bi^0 to UiO-66 through electrostatic interactions can induce a slight positive charge on the Bi atom. This reduces the electron density around Bi^0 NPs, but should increase the electron density around Zr ions [47]. As a result, in the composite, the XPS peaks corresponding to Bi^0 shifted to higher binding energies, while those for Zr ions shifted to lower binding energies, compared to those in pure UiO-66 and Bi^0.

Analysis of the N 1s spectra (Fig. 2f) revealed a weak peak at 400.5 eV in UiO-66, which could be attributed to residual DMF [55] on the surface. After calcination, this peak shifted to 400.1 eV and its intensity decreased, confirming DMF evaporation. In the 1.2 %Bi-UiO-66/TiO$_2$ sample, the N 1s peak shifted to 399.8 eV, and its intensity increased, likely due to the presence of some PVP in TiO$_2$ NFs.

Raman spectroscopy of the TiO$_2$ sample revealed the characteristic vibration peaks of TiO$_2$ anatase phase at 148.19 cm^{-1} (E_g), 198.2 cm^{-1} (E_g), 394.74 cm^{-1} (B_{1g}), 513.36 cm^{-1} ($A_{1g} + B_{1g}$), and 637.20 cm^{-1} (E_g) [56] (Fig. 3). After addition of 0.6 %, 0.9 %, and 1.2 % Bi(NO$_3$)$_3$, the vibration peaks became broader and were characterized by a slight blue shift of ~2.1 cm^{-1}. These changes can be attributed to the destruction of the anatase lattice, and formation of small amounts of brookite, and the

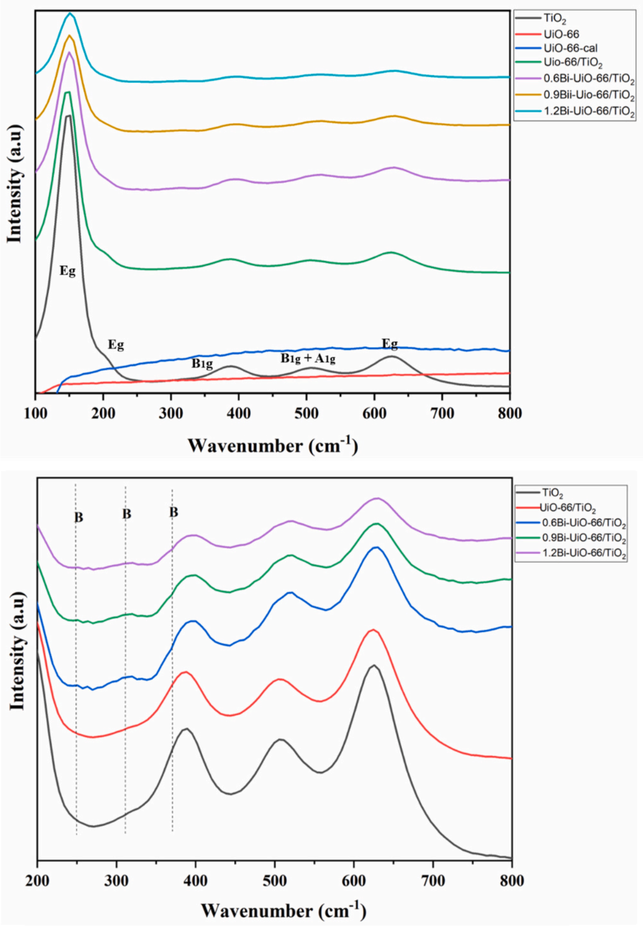

Fig. 3. Raman spectra of the indicated samples with the characteristic vibrational bands of the anatase and brookite phases.

effects of $Bi(NO_3)_3$-UiO-66 on the NF surface [57,58], which is consistent with the XRD data. The Raman spectra indicated that Bi ions influenced the phase transition, in line with the Rietveld refinement of the XRD results. In samples with higher $Bi(NO_3)_3$ amounts, the Raman bands progressively broadened and shifted to higher wavenumbers, particularly the E_g mode at 148.19 cm^{-1}. This shift is likely due to the crystallite size reduction [59]. Specifically, the NF volume concentration results in higher force constants that are associated with shorter interatomic distances. The increase in force constants was confirmed by the corresponding increase in the wavenumber that roughly correlated with the force constant [60]. The reduction in scattering intensity, especially for the E_g mode, can be attributed to defect-induced changes in the long-range translational crystal symmetry [61]. This may enhance the capture of photoelectrons, thereby reducing charge recombination. Additionally, the Bi NPs on the surface could further inhibit charge recombination by facilitating the transfer of photogenerated electrons to the pore surface [62].

The FT-IR results for UiO-66 (Fig. 4a) and TiO_2 (Fig. 4c) were consistent with those of previous works [63,64]. In the UiO-66 spectrum (Fig. 4a), the absorption band between 3000 and 3700 cm^{-1} was attributed to the stretching vibration of the hydroxyl groups from absorbed water molecules [65]. The peaks at 1627 cm^{-1} and 1576 and 1397 cm^{-1} corresponded to the -OH bending vibration [66] and the asymmetric and symmetric stretching vibration of carboxyl groups (O=C-O) [47,67], respectively. The weaker band at 1514 cm^{-1} was associated with the C=C vibration of the benzene ring [68]. The band at ~556 cm^{-1} was linked to the asymmetric stretching vibration of Zr–(OC) [69], while the peaks at ~668 and 482 cm^{-1} corresponded to the stretching vibrations of Zr–O$_{\mu3\text{-}O}$ and Zr–O$_{\mu3\text{-}OH}$ bonds in the Zr_6 cluster [70]. The peak at 747 cm^{-1} was attributed to C—H vibrations in BDC [50]. Additionally, the band at 1655 cm^{-1} (asymmetric stretching of the C=O bond in DMF) confirmed DMF presence in the pores [71]. In TiO_2 NF spectrum (Fig. 4c), a broad band was observed between 827 and 664 cm^{-1} that corresponded to the bending vibration of Ti–O–Ti [46]. The presence of these peaks in the spectra of UiO-66/TiO_2 (Fig. 4d) and Bi^0-UiO-66/TiO_2-Bi^{3+} NFs (Fig. 4e-g) confirmed that UiO-66 and Bi incorporation did not alter UiO-66 structure [72]. Additionally, the broad asymmetric peaks at 1603 cm^{-1} and 1397 cm^{-1}, observed after coupling TiO_2 NFs with UiO-66, were attributed to O=C-O stretching in UiO-66, while the band between 837 and 686 cm^{-1} corresponded to the Ti–O–Ti bond bending vibrations. The shift in these FT-IR spectra could be due to interactions between UiO-66, TiO_2 and Bi^{3+}. After Bi NP addition, no new peak was detected in the infrared spectrum of Bi-UiO-66/TiO_2, but the peak at 1603 cm^{-1} red-shifted to 1623 cm^{-1}, compared with UiO-66/TiO_2, suggesting a strong interaction between UiO-66 and Bi NPs [73]. In the composite samples, the decreased intensity of the characteristic peaks of UiO-66 and TiO_2 and their slight shift indicated changes in the chemical environment around UiO-66 and TiO_2, likely due to the interactions between TiO_2, $Bi(NO_3)_3$ and UiO-66. The FT-IR spectra confirmed that TiO_2, $Bi(NO_3)_3$ and UiO-66 formed strong interactions, demonstrating that the composite materials were successfully synthesized.

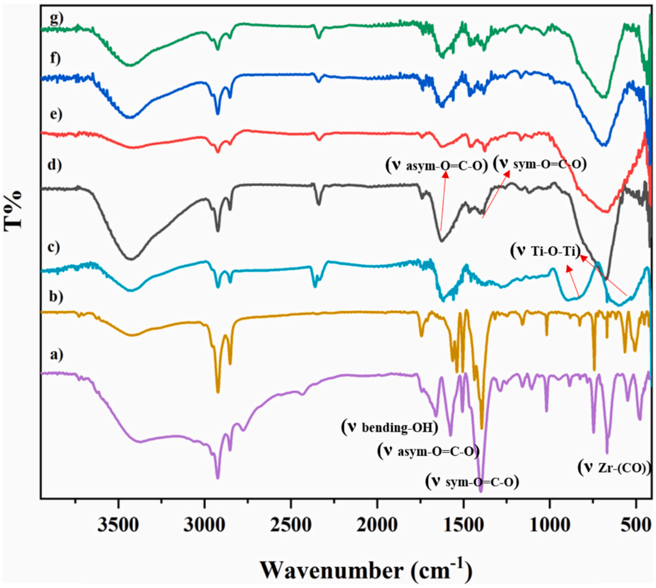

Fig. 4. FT-IR spectra of a) UiO-66, b) calcined UiO-66 (400 °C, 4 h), c) TiO_2, d) UiO-66/TiO_2, e) 0.6 %Bi-UiO-66/TiO_2, f) 0.9 %Bi-UiO-66/TiO_2, and g) 1.2 %Bi-UiO-66/TiO_2.

The results of the EDX analysis (Table S1) confirmed the incorporation of Zr and Bi into the TiO_2 NFs. The atomic ratios of Bi^{3+} to Ti^{4+} increased with higher amounts of $Bi(NO_3)_3$ (i.e., 1.2 > 0.9 > 0.6 mol%), consistent with the experimental findings. Elemental mapping images (Fig. S1) revealed that Bi and Zr ions were evenly distributed on TiO_2 surface.

SEM images (Fig. 5a-f) of Bi^0-UiO-66/TiO_2-Bi^{3+} revealed a highly interconnected network of continuous, but randomly oriented NFs. The incorporation of Bi ions into the composite material was confirmed by the NF diameter decrease from 188 ± 3 nm in pristine TiO_2 to 113 ± 3 nm in 1.2 %Bi-UiO-66/TiO_2 (Fig. S2). This reduction is in line with the decrease in crystallite size observed as the Bi^{3+} content increased (XRD data) and is attributed to the significant difference in ionic radius between Bi^{3+} and Ti^{4+} [41]. As a result, Bi cations cannot integrate the TiO_2 network, leading to disturbances in the anatase phase crystallites that ultimately hinder the crystallite structure growth [74].

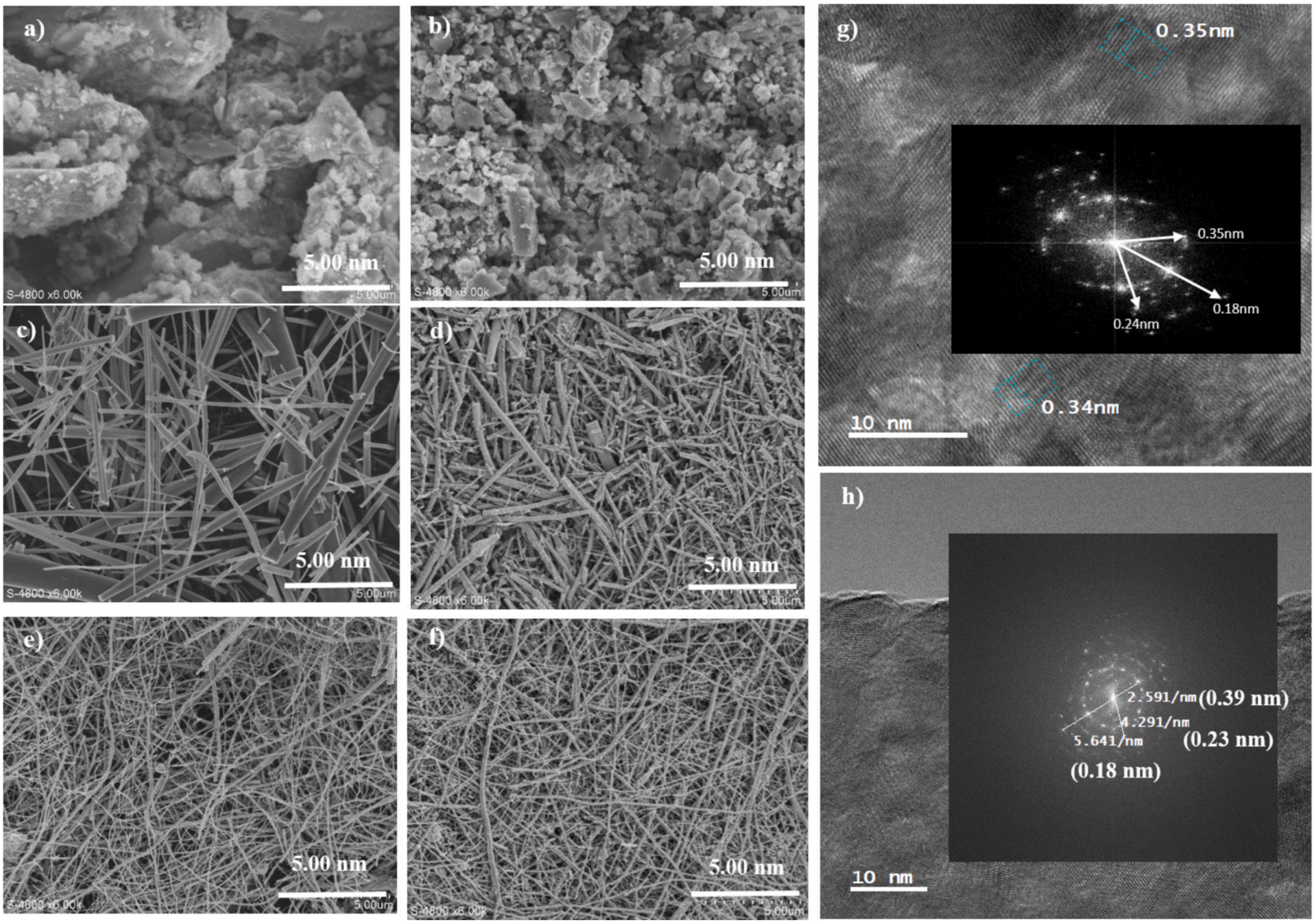

Fig. 5. SEM images of a) UiO-66, b) UiO-66 after calcination, c) TiO_2, d) 0.6 %Bi-UiO-66/TiO_2, e) 0.9 %Bi-UiO-66/TiO_2, f) 1.2 %Bi-UiO-66/TiO_2, and high-resolution TEM images of g) TiO_2 and h) 1.2 %Bi-UiO-66/TiO_2 with the diffraction patterns in the insets.

High-resolution TEM was employed to confirm the influence of Bi^0-UiO-66 and Bi_2O_3 on the TiO_2 phase structures (Fig. 5g-h). In TiO_2, the interplanar spacing values (0.35 ± 0.01 nm, 0.18 ± 0.01 nm, and 0.24 ± 0.01 nm) were associated with the (101), (211), and (004) planes of TiO_2 anatase (insets in Fig. 5g and h). In 1.2 %Bi-UiO-66/TiO_2, in addition to the interplanar spacing value of 0.18 ± 0.01 nm (corresponding to TiO_2 anatase), spacing values of 0.39 ± 0.01 nm (related to the (021) plane of α-Bi_2O_3 [75]) and 0.23 ± 0.01 nm (related to the (104) plane of rhombohedral Bi NP crystals [76]) were observed. The selected-area electron-diffraction and Fast Fourier Transform patterns of both samples (insets of Fig. 5g-h) confirmed the formation of a multi-phase mixture after Bi incorporation, indicating significant changes in crystallinity. The appearance of new planes (0.39 nm and 0.23 nm) suggests a modification in the crystal structure following the introduction of Bi^0 and Bi_2O_3.

The pore structure and specific surface areas were determined by N_2 adsorption-desorption measurements at 77 K. Brunauer-Emmett-Teller (BET) surface area measurements at 400 °C revealed an increase in the surface area from 45 $m^2\ g^{-1}$, 3.5 nm (TiO_2) to 53.7 $m^2\ g^{-1}$ (UiO-66/TiO_2) and to 92 $m^2\ g^{-1}$ (1.2 %Bi-UiO-66) (Table 2). In some systems, Bi incorporation may cause densification and reduce the surface area. However, in the present study, low Bi loading (1.2 %) combined with the high porosity of UiO-66 contributed to enhance surface accessibility. The introduction of Bi^0 NPs and Bi^{3+} ions may have improved the TiO_2 crystallite dispersion and prevented particle agglomeration, thereby increasing the available surface area. Moreover, Bi integration into the UiO-66/TiO_2 matrix might have contributed to maintain the MOF structure integrity, while introducing additional interfacial porosity. Collectively, these factors explain the BET surface area increase in the 1.2 %Bi–UiO-66/TiO_2 composite. However, the average pore volume was smaller than in other NFs, likely due to the insertion of Bi^0 NPs in UiO-66 pores and Bi^{3+} in TiO_2 pores. The *Barrett-Joyner-Halenda* (BJH) method confirmed the mesoporous nature of the materials (Table 2). The larger specific surface area of 1.2 %Bi-UiO-66/TiO_2 enhances the photocatalytic activity by facilitating the diffusion of reactants and products [77]. The high porosity of UiO-66 contributes to the nanocomposite surface area increase [78], thereby improving the photocatalytic performance [79]. These findings support the beneficial porous properties of UiO-66-based TiO_2 NFs. It can be concluded that the high porosity of UiO-66 crystallites contributes to the large surface area of the prepared composites [80]. The interfacial electron transfers in Bi-UiO-66/TiO_2

Table 2
Physical properties of UiO-66, calcined UiO-66, TiO_2 and Bi-doped-UiO-66/TiO_2 samples.

Samples	Surface area (BET) (m^2g^{-1})	Total pore volume (cm^3g^{-1})	Pore diameter (nm) (BJH)
TiO_2	45.0	0.1	3.5
Calcined UiO-66	400.6	0.27	5.1
UiO-66	37.9	0.02	4.5
1.2 %Bi-UiO-66/TiO_2	92.0	0.1	10.0–12.0
UiO-66/TiO_2	53.7	0.3	18.7

heterostructures might reduce the recombination of photoinduced e^-/h^+ pairs during photocatalysis. A photocatalyst with a larger specific surface area (BET measurements) provides more active sites, promoting efficient carrier transport and separation [81], thereby enhancing the efficiency of degradation reactions. However, the photocatalyst activity is also influenced by other factors, such as the crystallinity of the used materials and the stability of the charge carriers generated during the process.

The photoluminescence spectra of the TiO_2, UiO-66/TiO_2 and Bi-UiO-66/TiO_2 samples were examined to evaluate the e^-/h^+ pair separation rate and to determine the impact of Bi-UiO-66 introduction on charge separation. In TiO_2, the emission peak at 593 nm corresponded to the TiO_2 anatase reflection (Fig. 6a), and indicated a high recombination rate of e^-/h^+ pairs. In the UiO-66/TiO_2 sample, the emission intensity decreased, suggesting a better e^-/h^+ pair separation. Similarly, the photoluminescence intensity of Bi-UiO-66/TiO_2 samples (0.6 %, 0.9 %, and 1.2 % Bi) significantly decreased, especially that of the 1.2 %Bi-UiO-66/TiO_2 sample. This suggests that the formation of Bi^0-UiO-66/TiO_2-Bi^{3+} connections effectively reduces e^-/h^+ pair recombination, thereby enhancing the photocatalytic performance. Due to the higher work function of Bi (metal), the formation of Schottky barriers [34] facilitates electron transfer from UiO-66/TiO_2 to Bi (metal), which increases the separation of photogenerated e^-/h^+ pairs. In other words, Bi-UiO-66 helps to trap the photogenerated charge carriers and inhibits e^-/h^+ pair recombination [82]. Photoluminescence quenching in Bi-UiO-66-containing TiO_2 NFs can be attributed to the suppression of donor level formation within the TiO_2 band gap, such as charge transfer to excitons [83], which are responsible for TiO_2 photoluminescence [84].

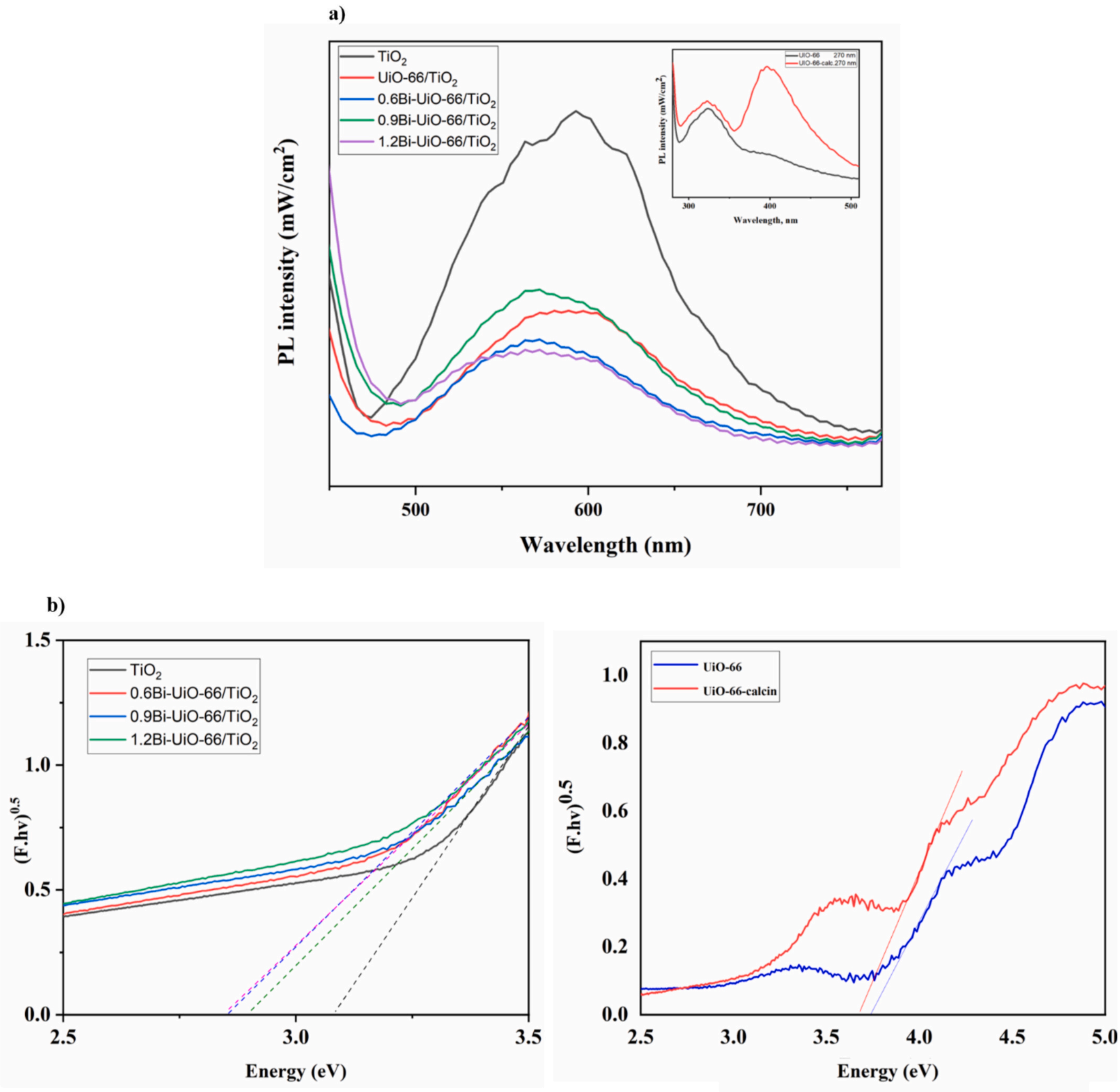

Fig. 6. **a)** Photoluminescence (PL) spectra of the indicated samples; inset: PL spectra of UiO-66 and calcined UiO-66. **b)** Curves of the transformed Kubelka–Munk function versus light energy to determine the band gap energy of the indicated samples.

The results indicate that the lifetime of free electrons is longer in pristine TiO_2 NFs than in Bi-UiO-66/TiO_2 NFs [85]. This explains the decrease in photoluminescence intensity of Bi-UiO-66/TiO_2 nanostructures. Therefore, Bi cations can enhance the photocatalytic activity by reducing charge recombination [86].

The band gap energy (Fig. 6b) was computed with the Kubelka-Munk formula [87]:

$$F = \left((1-R)^2\right) \Big/ 2R \tag{1}$$

$$(Fh\nu)^{1/2} = A(h\nu - Eg) \tag{2}$$

where F, R, hν, and Eg are the Kubelka–Munk function, reflectance, photon energy, and band gap, respectively.

Comparison of the Eg values of the different samples (Table 3) showed that it was decreased in the Bi-UiO-66/TiO_2 composites compared with TiO_2 and UiO-66/TiO_2.

Interestingly, after in-situ deposition of Bi (metallic), the photoinduced charge carriers can be efficiently separated due to the formation of Schottky barriers. Therefore, the enhanced photocatalytic efficiency of samples containing Bi (metallic) can be attributed to the improved separation of charge carrier [22].

The Urbach energy (E_{urb}) (Table 3) represents the width of the exponential absorption edge in the UV–Vis spectrum. It is typically associated with the presence of localized states due to structural disorder or defects in the material. Lower E_{urb} values indicate fewer defects and a more ordered structure, resulting in a sharper optical absorption edge. Conversely, higher E_{urb} values suggest increased disorder and sub-bandgap absorption that can influence the charge carrier dynamics and the overall photocatalytic performance.

3.2. H_2 generation

In this experimental set-up, methanol was employed as hole scavenger [88] *due to its strong tendency to donate electrons and its efficient oxidation by photogenerated holes. This suppresses* e^-/h^+ *recombination and enhances* H_2 *evolution. Methanol is often used as sacrificial agent in photocatalytic systems due to its low oxidation potential and good miscibility in aqueous media.* When pure TiO_2 was used as catalyst, H_2 production rate was low (110 μmol g^{-1} h^{-1}) (Fig. 7a). However, H_2 production rate increased progressively in the presence of Bi-UiO-66 on the surface of TiO_2 NFs. Higher concentrations of $Bi(NO_3)_3$ appear to promote the formation of heterojunctions between $Bi^0/Zr^{4+}/Bi^{3+}$ and TiO_2 that facilitate charge separation across the interfaces. The highest catalytic activity was achieved with the 1.2 %Bi-UiO-66/TiO_2 sample (H_2 evolution rate of 3734 $μmolg^{-1}$ h^{-1} versus 2852 $μmolg^{-1}h^{-1}$and 2162 $μmolg^{-1}h^{-1}$ with 0.9 %Bi-UiO-66/TiO_2 and 0.6 % Bi-UiO-66/TiO_2) (Fig. 7a). This improvement in performance can be attributed to its significantly higher surface area and large number of active sites.

The reusability and stability of the 1.2 %Bi-UiO-66/TiO_2 photocatalyst were evaluated over four consecutive cycles, each lasting 6 h under visible light irradiation (Fig. 7b). Comparison of *H_2 production after each cycle (bar chart in* Fig. 7b*) clearly demonstrated the photocatalyst excellent stability and retention of photocatalytic activity* (i.e. *reusability) over time.* Then, the structural stability of the 1.2 %Bi-UiO-66/TiO_2 photocatalyst after the catalytic reaction, was evaluated by XRD analysis. The XRD pattern (Fig. S3) showed no significant change between before and after use, confirming its good crystallinity and structural stability under reaction conditions.

Table 3
Band gap values of pure TiO_2 and Bi-UiO-66/TiO_2 NFs.

Sample	Band gap (eV)	Sample	Band gap (eV)/ E_{urb} (eV)
TiO_2	3.09	0.6 %Bi-UiO-66/ TiO_2	2.85/0.25
UiO-66	3. 63	0.9 %Bi-UiO-66/ TiO_2	2.8/0.29
Calcined UiO-66 (400 °C for 4 h)	3.58	1.2 %Bi-UiO-66/ TiO_2	2.83/0.31

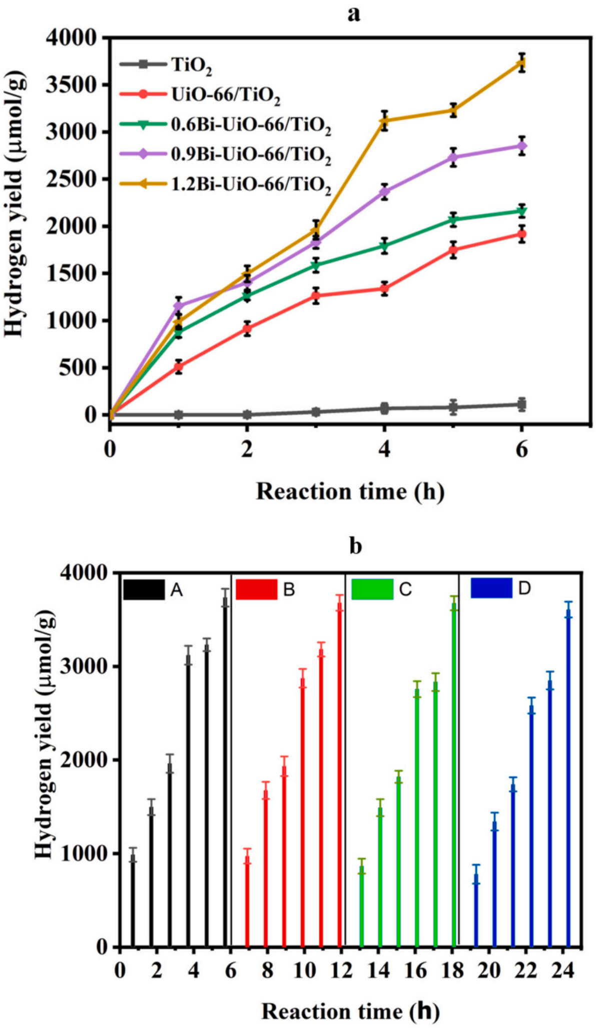

Fig. 7. **a)** H_2 production with the indicated photocatalysts. b) H_2 production in the presence of 1.2 % Bi-UiO-66/TiO_2 NFs after four cycles (A to D).

The photocatalytic activity of 1.2 %Bi-UiO-66/TiO_2 was comparable to or exceeded that of other UiO-66-containing photocatalysts tested in other works (Table 4). Its enhanced performance can be attributed to its high porosity and large surface area (90.9 m^2 g^{-1}) that provide a higher number of active sites and consequently facilitate more efficient e^-/h^+ pair separation. The modification of TiO_2 with Bi^{3+} and UiO-66 with Bi^0 improved the photocatalytic performance, primarily for two reasons. First, the gradual reduction of Bi^{3+} into Bi^0 (metallic) during synthesis led to the creation of oxygen vacancies, likely due to charge compensation [89]. In general, oxygen vacancies act as electron sinks by capturing excited electrons and promoting hole migration [90]. In Bi (M)-doped samples, electron transfer occurs through two pathways: Schottky barriers and oxygen vacancies. The photocatalytic experiments demonstrated that H_2 production in the presence of 1.2 %Bi-UiO-66/ TiO_2 (3734 $μmolg^{-1}$ h^{-1}) was significantly higher than the sum of the H_2 yields in the presence of UiO-66/TiO_2 (1920 $μmolg^{-1}$ h^{-1}) and TiO_2 (110 $μmolg^{-1}$ h^{-1}). This indicates a synergistic effect between Bi^{3+} and Bi^0, which was further supported by the UV–Vis and photoluminescence results. This synergist effect primarily results from two factors: i) the Schottky barrier, which facilitates efficient separation of photoinduced

Table 4
Hydrogen generation by different UiO-66-containing photocatalysts.

Catalyst	Preparation Technique	Output: H_2 production (μmol g^{-1} h^{-1})	Sacrificial agent	Reference	Light source
1.2 %Bi-3 %UiO-66/TiO_2	Electrospinning	3734	Methanol	This work	500 W linear halogen lamp
3 %UiO-66/TiO_2	Electrospinning	1918	Methanol	This work	500 W linear halogen lamp
Pt-loaded-UiO-66-Erythrosine B-sensitized-30	Hydrothermal	460	Methanol	[93]	300-W xenon lamp with a UV cut-off filter (λ > 420 nm)
Trimetallic MOF UiO66 (Zr/Ce/Ti)	Hydrothermal	9.5	–	[94]	UV–vis xenon lamp (150 mW cm-2) with/without filter (λ > 450 nm)
UiO-66@$ZnIn_2S_4$	Solvothermal	3061	Triethanolamine (TEOA)	[95]	300 W xenon lamp with a 400 nm cutoff filter
g-C_3N_4/UiO-66/Ni2P(50 %)	Hydrothermal	2000	Eosin Y (10 mg) in 30 mL TEOA (15 %)	[96]	5 W LED white light at 420 nm
UiO-66(Zr)-NH_2@UiO-66 (Ce)	Solvothermal	32	Methanol	[97]	150 W hg—Xe lamp equipped with a AM 1.5 G filter
UiO-66-PANI-Co_3O_4	Hydrothermal	710	TEOA	[98]	
16 %CdS/UiO-66	Hydrothermal	47,000	L-ascorbic acid (0.1 M, pH 4.0) and Pt (0.5 wt %) as co-catalyst	[99]	300-W xenon lamp with a UV cutoff filter (> 420 nm)
UiO-66-D@g-C_3N_4/Ni (2.0 %)	Solvothermal	2621	Aqueous 10 % (v/v) TEOA and eosin Y as photosensitizer	[100]	Simulated light irradiation (λ ≥ 420 nm)
UiO-66@g-C_3N_4/Ni		2057			

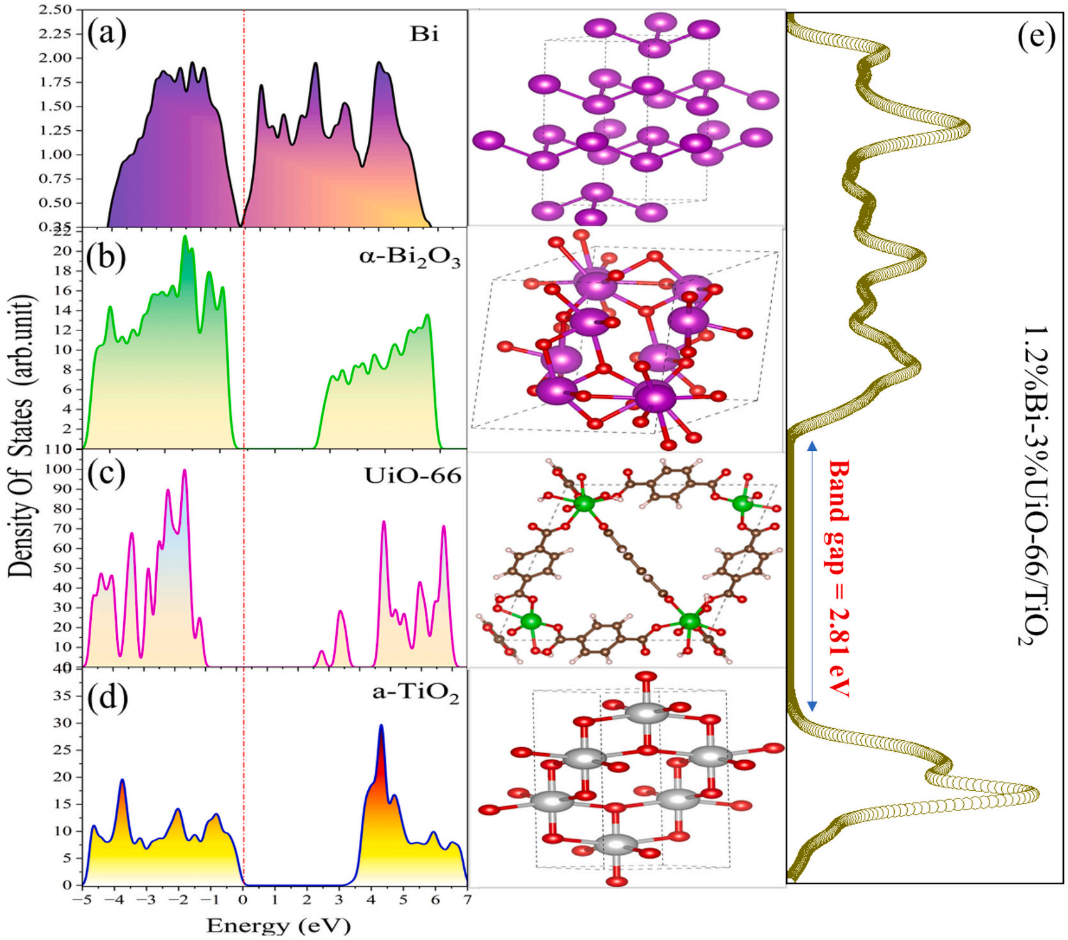

Fig. 8. a-d) Calculated total DOS of Bi, α-Bi_2O_3, UiO-66, and anatase TiO_2 (left panels) and their corresponding crystal structures (right panels), and e) DOS of 1.2 % Bi-UiO-66/TiO_2 NFs. Red dashed line, Fermi level.

charge carriers, and to a lesser extent, to the LSPR effect of Bi (metallic), which enhances visible light absorption; and ii) the reduction of band gap due to the presence of Bi^{3+}, leading to an increase in carrier density. As the band gap energy is calculated between the Bi^{3+} 6 s band top (due to lone pair electrons) and the Ti^{4+} 3d band bottom, it is narrower for 1.2 %Bi-UiO-66/TiO_2 than TiO_2. This is in agreement with the UV–vis diffuse reflectance spectroscopy data [24]. Furthermore, the incorporation of Bi^0 species into NFs helps to reduce e^-/h^+ pair recombination by trapping the photoinduced charge carriers, as indicated by the photoluminescence spectra. Therefore, the Bi 6 s level plays a key role in reducing the band gap energy and enhancing photocatalytic activity [91,92].

3.3. Mechanism

To gain a deeper understanding of the photocatalytic mechanism, DOS calculations were carried out for pure TiO_2 anatase, monoclinic α-Bi_2O_3, UiO-66, and 1.2 %Bi-UiO-66/TiO_2 (Fig. 8). Based on the calculated band gap values (3.12 eV, 2.78 eV, 3.42 eV, and 2.82 eV, respectively), these materials are categorized as semiconductors, with the exception of rhombohedral Bi, which is a gapless material. These values are consistent with both our experimental findings and previous literature data [101–104]. Notably, the band gap of the 1.2 %Bi-UiO-66/TiO_2 photocatalyst was smaller (2.82 eV) (Fig. 8e) than that of anatase TiO_2 and UiO-66, which can be attributed to the contribution of Bi-4d and Bi-6s electrons.

Our photocatalytic system consists of three semiconductors with Fermi levels near the valence band and one metallic material. Upon exposure to visible light, the absorbed energy promotes the formation of electrons, generating e^-/h^+ pairs. The presence of Bi, with its higher Fermi level, plays a key role in charge separation. It creates a built-in electric field at the interfaces that directs the photogenerated electrons toward the metal, due to the favorable energy gradient, and holes toward the semiconductor valence bands. This mechanism effectively reduces carrier recombination rates, leading to enhanced photocatalytic efficiency. Additionally, Bi may exhibits LSPR, which further enhances the local electric fields and improves light absorption.

Photocatalytic water splitting with Bi-UiO-66/TiO_2 NFs led to a H_2 yield of 3734 μmolg^{-1} h^{-1}, significantly surpassing the performance of UiO-66/TiO_2 and pure TiO_2 (1918 μmolg^{-1} h^{-1} and 110 μmolg^{-1} h^{-1}, respectively). A plausible mechanism for water splitting under visible light in the presence of Bi^0-UiO-66/TiO_2-Bi^{3+} can be proposed (Fig. 9). Initially, photoexcitation generates electrons and holes in the Bi_2O_3 component. Electrons migrate to TiO_2 and holes to Bi_2O_3. This charge separation creates active sites in the conduction bands of Bi_2O_3 and TiO_2, facilitating H_2 generation through photogenerated e^-/h^+ recombination. Electrons are transferred from TiO_2 to Bi clusters. At the TiO_2/UiO-66 interface, the photoinduced charge carriers are trapped in defect states, and electrons migrate toward the adsorbed O_2 and holes toward Bi_2O_3. The UiO-66-TiO_2 heterojunction promotes e^-/h^+ pair separation, which contributes to improve the photocatalytic activity [65]. Notably, after in-situ deposition of Bi (metallic), the photoinduced charge carriers are effectively separated due to the formation a Schottky barrier. Furthermore, Bi^0 NPs enhance the visible light response and reduce carrier recombination through the LSPR effect.

4. Conclusion

Novel Bi^0-UiO-66/TiO_2-Bi^{3+} photocatalysts were successfully synthesized using a simple one-step approach. FT-IR characterization revealed that the original crystal structures of TiO_2 and UiO-66/TiO_2 were not altered in the Bi^0/Bi^{3+}-modified composites. The XPS spectra confirmed the co-existence of both Bi^{3+} and Bi (metallic) in the Bi^0-UiO-66/TiO_2-Bi^{3+} composites. The high-resolution TEM images, Raman spectra and XRD results further supported the presence of both anatase and brookite phases in the composite NFs. Additionally, the specific surface area of the photocatalysts modified with Bi^{3+} and Bi (metallic) was significantly enhanced, contributing to their improved photocatalytic performance. The photocatalytic experiments demonstrated that H_2 generation in the presence of Bi^0-UiO-66/TiO_2-Bi^{3+} (3734 μmolg^{-1} h^{-1}) was significantly higher than the sum of the H_2 yields in the presence of TiO_2 (110 μmolg^{-1} h^{-1}) and UiO-66/TiO_2 (1920 μmolg^{-1} h^{-1}). This synergistic effect of Bi^{3+} and Bi (metallic) was further validated by the UV–Vis and photoluminescence results. Specifically, Bi^0 NPs enhanced the visible light absorption and inhibited charge carrier recombination through the LSPR effect, as also supported by the DFT simulations. Moreover, Bi^0-UiO-66/TiO_2-Bi^{3+} exhibited outstanding reusability and stability. This study presents novel strategies to enhance the photocatalytic performance of Bi-based materials without introducing any impurity. It also lays the foundation for

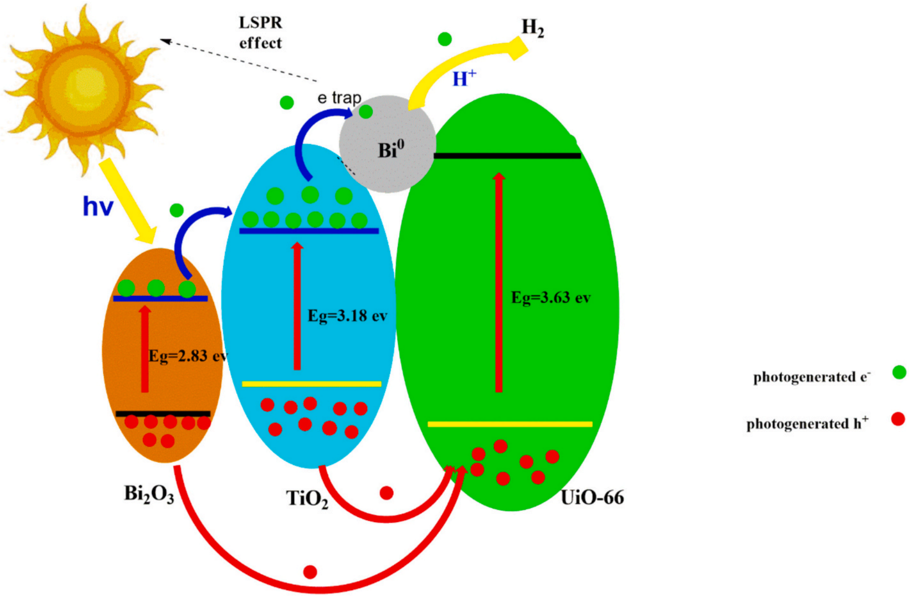

Fig. 9. Schematic illustration and suggested mechanism of electron-hole pair transfer and separation in the Bi^0-UiO-66/TiO_2-Bi^{3+} NF system for photocatalytic H_2 production under visible light.

designing MOF-based heterostructures that can serve as advanced photocatalysts, thanks to the increased number of active sites and favorable optical properties, making them ideal for various environmental applications.

CRediT authorship contribution statement

Mitra Saffari: Writing – original draft, Validation, Formal analysis, Data curation, Conceptualization. **Massomeh Ghorbanloo:** Writing – review & editing, Visualization, Validation, Supervision, Methodology, Conceptualization. **Ali Morsali:** Writing – review & editing, Validation, Supervision. **Heba H. Elmaghrabi:** Writing – review & editing, Validation, Formal analysis, Data curation. **Djamel Bezzerga:** Writing – review & editing, Validation, Investigation, Formal analysis, Data curation. **Jisang Hong:** Writing – review & editing, Validation, Supervision, Formal analysis. **Tia Maria Howayek:** Writing – review & editing, Visualization, Validation, Formal analysis, Data curation. **Roland Habchi:** Writing – review & editing, Validation, Supervision, Formal analysis. **Roman Viter:** Writing – review & editing, Visualization, Validation, Formal analysis, Data curation. **Bernard Fraisse:** Writing – review & editing, Validation, Formal analysis, Data curation. **Igor Iatsunskyi:** Writing – review & editing, Validation, Formal analysis, Data curation. **Emerson Coy:** Writing – review & editing, Validation, Formal analysis, Data curation. **David Cornu:** Writing – review & editing, Validation, Supervision, Formal analysis. **Amr A. Nada:** Writing – review & editing, Validation, Supervision, Formal analysis, Conceptualization. **Mikhael Bechelany:** Writing – review & editing, Validation, Supervision, Resources, Formal analysis, Conceptualization.

Declaration of competing interest

The authors declare that they have no known competing financial interests or personal relationships that could have appeared to influence the work reported in this paper.

Acknowledgments

University of Zanjan financially supported this study. D. B. and J. H. acknowledge the National Research Foundation of Korea (NRF) support through a Korean government grant (MSIT) (grant number 2022R1A2C1004440).

Appendix A. Supplementary data

Supplementary data to this article can be found online at https://doi.org/10.1016/j.jphotochem.2025.116667.

Data availability

Data will be made available on request.

References

[1] X. Zhang, L. Li, Q. Zhou, X. Liang, D. Liu, Facile synthesis of novel gully-like double-sized mesoporous structural Sr-doped ZrO2–TiO2 composites with improved photocatalytic efficiency, J. Solid State Chem. 269 (2019) 375–385.

[2] C. Gao, J. Wang, H. Xu, Y. Xiong, Coordination chemistry in the design of heterogeneous photocatalysts, Chem. Soc. Rev. 46 (2017) 2799–2823.

[3] K. Yu, C. Zhang, Y. Chang, Y. Feng, Z. Yang, T. Yang, L.-L. Lou, S. Liu, Novel three-dimensionally ordered macroporous SrTiO3 photocatalysts with remarkably enhanced hydrogen production performance, Appl. Catal. B Environ. 200 (2017) 514–520.

[4] J. Zhang, L. Li, Z. Xiao, D. Liu, S. Wang, J. Zhang, Y. Hao, W. Zhang, Hollow sphere TiO2–ZrO2 prepared by self-assembly with polystyrene colloidal template for both photocatalytic degradation and H2 evolution from water splitting, ACS Sustain. Chem. Eng. 4 (2016) 2037–2046.

[5] S. Kreft, D. Wei, H. Junge, M. Beller, Recent advances on TiO2-based photocatalytic CO2 reduction, EnergyChem 2 (2020) 100044.

[6] R. Franking, L. Li, M.A. Lukowski, F. Meng, Y. Tan, R.J. Hamers, S. Jin, Facile post-growth doping of nanostructured hematite photoanodes for enhanced photoelectrochemical water oxidation, Energy Environ. Sci. 6 (2013) 500–512.

[7] Z. Lei, Y. Xue, W. Chen, W. Qiu, Y. Zhang, S. Horike, L. Tang, MOFs-based heterogeneous catalysts: new opportunities for energy-related CO2 conversion, Adv. Energy Mater. 8 (2018) 1801587.

[8] Y. Wang, H. Jin, Q. Ma, K. Mo, H. Mao, A. Feldhoff, X. Cao, Y. Li, F. Pan, Z. Jiang, A MOF glass membrane for gas separation, Angew. Chem. 132 (2020) 4395–4399.

[9] B.M. Connolly, D.G. Madden, A.E. Wheatley, D. Fairen-Jimenez, Shaping the future of fuel: monolithic metal–organic frameworks for high-density gas storage, J. Am. Chem. Soc. 142 (2020) 8541–8549.

[10] H.A. Younes, M. Taha, R. Mahmoud, H.M. Mahmoud, R.M. Abdelhameed, High adsorption of sodium diclofenac on post-synthetic modified zirconium-based metal-organic frameworks: experimental and theoretical studies, J. Colloid Interface Sci. 607 (2022) 334–346.

[11] T. Xia, Y. Lin, W. Li, M. Ju, Photocatalytic degradation of organic pollutants by MOFs based materials: a review, Chin. Chem. Lett. 32 (2021) 2975–2984.

[12] S. Yuan, L. Feng, K. Wang, J. Pang, M. Bosch, C. Lollar, Y. Sun, J. Qin, X. Yang, P. Zhang, Stable metal–organic frameworks: stable metal–organic frameworks: design, synthesis, and applications (Adv. Mater. 37/2018), Adv. Mater. 30 (2018) 1870277.

[13] N. Yuan, X. Gong, W. Sun, C. Yu, Advanced applications of Zr-based MOFs in the removal of water pollutants, Chemosphere 267 (2021) 128863.

[14] G. Zhang, L. Jin, R. Zhang, Y. Bai, R. Zhu, H. Pang, Recent advances in the development of electronically and ionically conductive metal-organic frameworks, Coord. Chem. Rev. 439 (2021) 213915.

[15] C. Cheng, J. Fang, S. Lu, C. Cen, Y. Chen, L. Ren, W. Feng, Z. Fang, Zirconium metal-organic framework supported highly-dispersed nanosized BiVO4 for enhanced visible-light photocatalytic applications, J. Chem. Technol. Biotechnol. 91 (2016) 2785–2792.

[16] M. Taddei, G.M. Schukraft, M.E. Warwick, D. Tiana, M.J. McPherson, D.R. Jones, C. Petit, Band gap modulation in zirconium-based metal–organic frameworks by defect engineering, J Mater Chem A 7 (2019) 23781–23786.

[17] J. Qiu, X. Zhang, K. Xie, X.-F. Zhang, Y. Feng, M. Jia, J. Yao, Noble metal nanoparticle-functionalized Zr-metal organic frameworks with excellent photocatalytic performance, J. Colloid Interface Sci. 538 (2019) 569–577.

[18] S. Subudhi, L. Paramanik, S. Sultana, S. Mansingh, P. Mohapatra, K. Parida, A type-II interband alignment heterojunction architecture of cobalt titanate integrated UiO-66-NH2: a visible light mediated photocatalytic approach directed towards Norfloxacin degradation and green energy (hydrogen) evolution, J. Colloid Interface Sci. 568 (2020) 89–105.

[19] F. Zhang, W. Cheng, Z. Yu, S. Ge, Q. Shao, D. Pan, B. Liu, X. Wang, Z. Guo, Microwave hydrothermally synthesized WO 3/UiO-66 nanocomposites toward enhanced photocatalytic degradation of rhodamine B, Adv. Compos. Hybrid Mater. 4 (2021) 1330–1342.

[20] X. He, Y. Guo, J. Zhang, S. Yang, J. Chen, S. Li, S. Xie, Y. Wang, C. Wang, Why can poorly conductive Bi@ UiO-MOF catalyze CO 2 electroreduction? Chem. Commun. 59 (2023) 5737–5740.

[21] H. Liu, H. Mei, N. Miao, L. Pan, Z. Jin, G. Zhu, J. Gao, J. Wang, Synergistic photocatalytic NO removal of oxygen vacancies and metallic bismuth on Bi12TiO20 nanofibers under visible light irradiation, Chem. Eng. J. 414 (2021) 128748.

[22] Q. Wu, S. Chai, H. Yang, Z. Gao, R. Zhang, L. Wang, L. Kang, Enhancing visible-light driven photocatalytic performance of BiOBr by self-doping and in-situ deposition strategy: a synergistic effect between Bi5+ and metallic Bi, Sep. Purif. Technol. 253 (2020) 117388.

[23] F. Dong, T. Xiong, Y. Sun, Z. Zhao, Y. Zhou, X. Feng, Z. Wu, A semimetal bismuth element as a direct plasmonic photocatalyst, Chem. Commun. 50 (2014) 10386–10389.

[24] J. Xu, W. Wang, M. Shang, E. Gao, Z. Zhang, J. Ren, Electrospun nanofibers of Bi-doped TiO2 with high photocatalytic activity under visible light irradiation, J. Hazard. Mater. 196 (2011) 426–430.

[25] Y. Wu, G. Lu, S. Li, The doping effect of Bi on TiO2 for photocatalytic hydrogen generation and photodecolorization of rhodamine B, J. Phys. Chem. C 113 (2009) 9950–9955.

[26] Q. Zhao, W. Yuan, J. Liang, J. Li, Synthesis and hydrogen storage studies of metal– organic framework UiO-66, Int. J. Hydrog. Energy 38 (2013) 13104–13109.

[27] M. Ghorbanloo, A.A. Nada, H.H. El-Maghrabi, M.F. Bekheet, W. Riedel, R. Viter, S. Roualdes, P. Miele, M. Bechelany, BN/Cs2CO3/TiO2 composite nanofibers to improve hydrogen generation, J. Alloys Compd. 945 (2023) 169218.

[28] M. Mehdikhanloo, Z. Hagheh-Kavousi, M. Ghorbanloo, A.A. Nada, H.H. El-Maghrabi, R. Hosny, F. Zahran, R. Viter, D. Bezzerga, J. Hong, Influence of interface defects and Zr doping on the photocatalytic activity of TiO2 nanofibers in water splitting, J. Alloys Compd. 179439 (2025).

[29] M. Ghorbanloo, A.A. Nada, H.H. El-Maghrabi, M.F. Bekheet, W. Riedel, B. Djamel, R. Viter, S. Roualdes, F.S. Soliman, Y.M. Moustafa, Superior efficiency of BN/Ce2O3/TiO2 nanofibers for photocatalytic hydrogen generation reactions, Appl. Surf. Sci. 594 (2022) 153438.

[30] M. Saffari, Z.H. Kavousi, M. Ghorbanloo, A.A. Nada, M.F. Bekheet, D. Bezzerga, J. Hong, A. Morsali, Y. Holade, R. Viter, Copper benzene-1, 3, 5-tricarboxylate based metal organic framework (MOF) derived CuO/TiO2 nanofibers and their use as visible light active photocatalyst for the hydrogen production, Appl. Surf. Sci. 678 (2024) 161061.

[31] D.A. Shirley, High-resolution X-ray photoemission spectrum of the valence bands of gold, Phys. Rev. B 5 (1972) 4709.

[32] J.H. Scofield, Hartree-slater subshell photoionization cross-sections at 1254 and 1487 eV, J. Electron Spectrosc. Relat. Phenom. 8 (1976) 129–137.

[33] A.A. Nada, M. Nasr, R. Viter, P. Miele, S. Roualdes, M. Bechelany, Mesoporous ZnFe2O4@ TiO2 nanofibers prepared by electrospinning coupled to PECVD as highly performing photocatalytic materials, J. Phys. Chem. C 121 (2017) 24669–24677.

[34] J.P. Perdew, A. Ruzsinszky, G.I. Csonka, O.A. Vydrov, G.E. Scuseria, L. A. Constantin, X. Zhou, K. Burke, Restoring the density-gradient expansion for exchange in solids and surfaces, Phys. Rev. Lett. 100 (2008) 136406.

[35] T.S. El-Shazly, W.M. Hassan, S.S.A. Rehim, N.K. Allam, DFT insights into the electronic and optical properties of fluorine-doped monoclinic niobium pentoxide (B-Nb 2 O 5: F), Appl. Phy. A 122 (2016) 1–7.

[36] P. Giannozzi, O. Andreussi, T. Brumme, O. Bunau, M.B. Nardelli, M. Calandra, R. Car, C. Cavazzoni, D. Ceresoli, M. Cococcioni, Advanced capabilities for materials modelling with quantum ESPRESSO, J. Phys. Condens. Matter 29 (2017) 465901.

[37] Y. Zhang, H. Jiang, Intra-and interatomic spin interactions by the density functional theory plus U approach: a critical assessment, J. Chem. Theory Comput. 7 (2011) 2795–2803.

[38] V. Yadav, V. Kulshrestha, Boron nitride: a promising material for proton exchange membranes for energy applications, Nanoscale 11 (2019) 12755–12773.

[39] Q. Tay, X. Liu, Y. Tang, Z. Jiang, T.C. Sum, Z. Chen, Enhanced photocatalytic hydrogen production with synergistic two-phase anatase/brookite TiO2 nanostructures, J. Phys. Chem. C 117 (2013) 14973–14982.

[40] H. Molavi, M. Zamani, M. Aghajanzadeh, H. Kheiri Manjili, H. Danafar, A. Shojaei, Evaluation of UiO-66 metal organic framework as an effective sorbent for curcumin's overdose, Appl. Organomet. Chem. 32 (2018) e4221.

[41] R.D. Shannon, Revised effective ionic radii and systematic studies of interatomic distances in halides and chalcogenides, Acta Crystallogr. Sect. A: Cryst. Phys., Diffr., Theor. Gen. Crystallogr. 32 (1976) 751–767.

[42] S. Estrada-Flores, C.M. Pérez-Berumen, T.E. Flores-Guia, L.A. García-Cerda, J. Rodríguez-Hernández, T.A. Esquivel-Castro, A. Martínez-Luévanos, Mechanosynthesis of mesoporous Bi-doped TiO2: the effect of bismuth doping and ball milling on the crystal structure, optical properties, and photocatalytic activity, Crystals 12 (2022) 1750.

[43] X. Zhang, Z. Zhang, M. Xu, S. Zhou, R. Sun, X. Liang, F. Wang, M. Chen, Topology engineering of UiO-66@ TiO2-based photoelectrocatalyst for highly efficient degradation of binary pollutants, Sep. Purif. Technol. 330 (2024) 125437.

[44] Z.-W. Wang, K.-W. Chen, A.-T. Gu, X.-Y. Zhou, P. Wang, C.-H. Gong, P. Mao, Y. Jiao, K. Chen, J.-G. Lu, Adsorption performance study of bismuth-doped ZIF-8 composites on radioactive iodine in the vapor and liquid phases, J. Solid State Chem. 325 (2023) 124186.

[45] K.K. Mandari, A.K.R. Police, J.Y. Do, M. Kang, C. Byon, Rare earth metal Gd influenced defect sites in N doped TiO2: defect mediated improved charge transfer for enhanced photocatalytic hydrogen production, Int. J. Hydrog. Energy 43 (2018) 2073–2082.

[46] J. Wang, Z. Sun, X. Jiang, Q. Yuan, D. Dong, P. Zhang, Z. Zhang, Uniform decoration of UiO-66-NH 2 nanooctahedra on TiO 2 electrospun nanofibers for enhancing photocatalytic H 2 production based on multi-step interfacial charge transfer, Dalton Trans. 50 (2021) 6152–6160.

[47] L. Wu, Y. Luo, C. Wang, S. Wu, Y. Zheng, Z. Li, Z. Cui, Y. Liang, S. Zhu, J. Shen, Self-driven electron transfer biomimetic enzymatic catalysis of bismuth-doped PCN-222 MOF for rapid therapy of bacteria-infected wounds, ACS Nano 17 (2023) 1448–1463.

[48] X. Ren, S. Yang, N. Yu, A. Sharjeel, Q. Jiang, D.K. Macharia, H. Yan, C. Lu, P. Geng, Z. Chen, Cell membrane camouflaged bismuth nanoparticles for targeted photothermal therapy of homotypic tumors, J. Colloid Interface Sci. 591 (2021) 229–238.

[49] N. Albayati, M. Kadhom, Preparation of functionalised UiO-66 metal–organic frameworks (MOFs) nanoparticles using deep eutectic solvents as a benign medium, Micro Nano Lett. 15 (2020) 1075–1078.

[50] C. Chen, D. Chen, S. Xie, H. Quan, X. Luo, L. Guo, Adsorption behaviors of organic micropollutants on zirconium metal–organic framework UiO-66: analysis of surface interactions, ACS Appl. Mater. Interfaces 9 (2017) 41043–41054.

[51] Q. Wang, T. Niu, L. Wang, C. Yan, J. Huang, J. He, H. She, B. Su, Y. Bi, FeF2/BiVO4 heterojuction photoelectrodes and evaluation of its photoelectrochemical performance for water splitting, Chem. Eng. J. 337 (2018) 506–514.

[52] Y. Lin, D. Pan, H. Luo, Hollow direct Z–Scheme CdS/BiVO4 composite with boosted photocatalytic performance for RhB degradation and hydrogen production, Mater. Sci. Semicond. Process. 121 (2021) 105453.

[53] D. Briggs, Practical surface analysis, Auger X-Ray Photoelecton. Spectro. 1 (1990) 151–152.

[54] J. Chastain, R.C. King Jr., Handbook of X-ray photoelectron spectroscopy, Perkin-Elmer Corporation 40 (1992) 221.

[55] X. Lü, J. Shen, Z. Wu, J. Wang, J. Xie, Deposition of ag nanoparticles on g-C3N4 nanosheet by N, N-dimethylformamide: soft synthesis and enhanced photocatalytic activity, J. Mater. Res. 29 (2014) 2170–2178.

[56] J. Wang, P. Wang, Y. Cao, J. Chen, W. Li, Y. Shao, Y. Zheng, D. Li, A high efficient photocatalyst Ag3VO4/TiO2/graphene nanocomposite with wide spectral response, Appl. Catal. B Environ. 136 (2013) 94–102.

[57] S.D. Perera, R.G. Mariano, K. Vu, N. Nour, O. Seitz, Y. Chabal, K.J. Balkus Jr., Hydrothermal synthesis of graphene-TiO2 nanotube composites with enhanced photocatalytic activity, ACS Catal. 2 (2012) 949–956.

[58] A.A. Nada, M.F. Bekheet, R. Viter, P. Miele, S. Roualdes, M. Bechelany, BN/GdxTi (1-x) O (4-x)/2 nanofibers for enhanced photocatalytic hydrogen production under visible light, Appl. Catal. B Environ. 251 (2019) 76–86.

[59] L. Xu, X. Ma, N. Sun, F. Chen, Bulk oxygen vacancies enriched TiO2 and its enhanced visible photocatalytic performance, Appl. Surf. Sci. 441 (2018) 150–155.

[60] H.C. Choi, Y.M. Jung, S.B. Kim, Size effects in the Raman spectra of TiO2 nanoparticles, Vib. Spectrosc. 37 (2005) 33–38.

[61] C.-W. Huang, B.-J. Lin, H.-Y. Lin, C.-H. Huang, F.-Y. Shih, W.-H. Wang, C.-Y. Liu, H.-C. Chui, Observation of strain effect on the suspended graphene by polarized Raman spectroscopy, Nanoscale Res. Lett. 7 (2012) 1–6.

[62] S. Sajjad, S.A. Leghari, F. Chen, J. Zhang, Bismuth-doped ordered mesoporous TiO2: visible-light catalyst for simultaneous degradation of phenol and chromium, chemistry–a, Eur. J. Dermatol. 16 (2010) 13795–13804.

[63] X. Zhang, Y. Yang, W. Huang, Y. Yang, Y. Wang, C. He, N. Liu, M. Wu, L. Tang, G-C3N4/UiO-66 nanohybrids with enhanced photocatalytic activities for the oxidation of dye under visible light irradiation, Mater. Res. Bull. 99 (2018) 349–358.

[64] J. Lei, Y. Chen, F. Shen, L. Wang, Y. Liu, J. Zhang, Surface modification of TiO2 with g-C3N4 for enhanced UV and visible photocatalytic activity, J. Alloys Compd. 631 (2015) 328–334.

[65] Z. Man, Y. Meng, X. Lin, X. Dai, L. Wang, D. Liu, Assembling UiO-66@ TiO2 nanocomposites for efficient photocatalytic degradation of dimethyl sulfide, Chem. Eng. J. 431 (2022) 133952.

[66] Y. Ma, Q. Tang, W.-Y. Sun, Z.-Y. Yao, W. Zhu, T. Li, J. Wang, Assembling ultrafine TiO2 nanoparticles on UiO-66 octahedrons to promote selective photocatalytic conversion of CO2 to CH4 at a low concentration, Appl. Catal. B Environ. 270 (2020) 118856.

[67] Z. Wang, J. Yang, Y. Li, Q. Zhuang, J. Gu, Simultaneous degradation and removal of CrVI from aqueous solution with Zr-based metal–organic frameworks bearing inherent reductive sites, Chem. A Eur. J. Dermatol. 23 (2017) 15415–15423.

[68] G.Y. Shangkum, P. Chammingkwan, D.X. Trinh, T. Taniike, Design of a semi-continuous selective layer based on deposition of UiO-66 nanoparticles for nanofiltration, Membranes 8 (2018) 129.

[69] J. Ding, Z. Yang, C. He, X. Tong, Y. Li, X. Niu, H. Zhang, UiO-66 (Zr) coupled with Bi2MoO6 as photocatalyst for visible-light promoted dye degradation, J. Colloid Interface Sci. 497 (2017) 126–133.

[70] Y. Han, M. Liu, K. Li, Y. Zuo, Y. Wei, S. Xu, G. Zhang, C. Song, Z. Zhang, X. Guo, Facile synthesis of morphology and size-controlled zirconium metal–organic framework UiO-66: the role of hydrofluoric acid in crystallization, CrystEngComm 17 (2015) 6434–6440.

[71] A.S. Abdelmoaty, S.T. El-Wakeel, N. Fathy, A.A. Hanna, High performance of UiO-66 metal–organic framework modified with melamine for uptaking of lead and cadmium from aqueous solutions, J. Inorg. Organomet. Polym. Mater. 32 (2022) 2557–2567.

[72] Y. Liu, Y. Xu, D. Zhong, N. Zhong, Visible-light photocatalytic fuel cell with BiVO4/UiO-66/TiO2/Ti photoanode efficient degradation of rhodamine B and stable generation of electricity, Chem. Phys. 542 (2021) 111053.

[73] L. Li, X. Yu, L. Xu, Y. Zhao, Fabrication of a novel type visible-light-driven heterojunction photocatalyst: metal-porphyrinic metal organic framework coupled with PW12/TiO2, Chem. Eng. J. 386 (2020) 123955.

[74] S.M. Adyani, M. Ghorbani, A comparative study of physicochemical and photocatalytic properties of visible light responsive Fe, Gd and P single and tri-doped TiO2 nanomaterials, J. Rare Earths 36 (2018) 72–85.

[75] A.K. Berekute, K.-P. Yu, Y.-H.B. Chuang, Enhanced photocatalytic activity of novel α-Bi2O3@ g-C3N4 composites for the degradation of endocrine-disrupting benzophenone-3 in water under visible light, Sustain. Environ. Res. 32 (2022) 17.

[76] X. Chang, S. Wang, Q. Qi, M.A. Gondal, S.G. Rashid, S. Gao, D. Yang, K. Shen, Q. Xu, P. Wang, Insights into the growth of bismuth nanoparticles on 2D structured BiOCl photocatalysts: an in situ TEM investigation, Dalton Trans. 44 (2015) 15888–15896.

[77] Y. Zhang, L. Liu, L. Zhao, C. Hou, M. Huang, H. Algadi, D. Li, Q. Xia, J. Wang, Z. Zhou, Sandwich-like CoMoP2/MoP heterostructures coupling N, P co-doped carbon nanosheets as advanced anodes for high-performance lithium-ion batteries, Adv. Compos. Hybrid Mater. 5 (2022) 2601–2610.

[78] X. Hou, S.L. Stanley, M. Zhao, J. Zhang, H. Zhou, Y. Cai, F. Huang, Q. Wei, MOF-based C-doped coupled TiO2/ZnO nanofibrous membrane with crossed network connection for enhanced photocatalytic activity, J. Alloys Compd. 777 (2019) 982–990.

[79] C. Hou, W. Yang, H. Kimura, X. Xie, X. Zhang, X. Sun, Z. Yu, X. Yang, Y. Zhang, B. Wang, Boosted lithium storage performance by local build-in electric field derived by oxygen vacancies in 3D holey N-doped carbon structure decorated with molybdenum dioxide, J. Mater. Sci. Technol. 142 (2023) 185–195.

[80] J. Zhao, D.T. Lee, R.W. Yaga, M.G. Hall, H.F. Barton, I.R. Woodward, C. J. Oldham, H.J. Walls, G.W. Peterson, G.N. Parsons, Ultra-fast degradation of chemical warfare agents using MOF–nanofiber kebabs, Angew. Chem. 128 (2016) 13418–13422.

[81] T. Li, J.-D. Cui, M.-L. Xu, R. Li, L.-M. Gao, P.-L. Zhu, H.-Q. Xie, K. Li, Engineering a hetero-MOF-derived TiO 2–co 3 O 4 heterojunction decorated with nickel nanoparticles for enhanced photocatalytic activity even in pure water, CrystEngComm 22 (2020) 5620–5627.

[82] X. Wang, R.L. Patel, X. Liang, Significant improvement in TiO 2 photocatalytic activity through controllable ZrO 2 deposition, RSC Adv. 8 (2018) 25829–25834.

[83] J. Dhanalakshmi, S. Iyyapushpam, S. Nishanthi, M. Malligavathy, D.P. Padiyan, Investigation of oxygen vacancies in Ce coupled TiO2 nanocomposites by Raman and PL spectra, Adv. Nat. Sci. Nanosci. Nanotechnol. 8 (2017) 015015.

[84] M. Nasr, R. Viter, C. Eid, R. Habchi, P. Miele, M. Bechelany, Enhanced photocatalytic performance of novel electrospun BN/TiO 2 composite nanofibers, New J. Chem. 41 (2017) 81–89.

[85] H. Zong, Y.-H. Lou, M. Li, K.-L. Wang, S.M. Jain, Z.-K. Wang, Improved open-circuit voltage via Cs2CO3-doped TiO2 for high-performance and stable perovskite solar cells, Org. Electron. 77 (2020) 105495.

[86] P.A.K. Reddy, B. Srinivas, P. Kala, V.D. Kumari, M. Subrahmanyam, Preparation and characterization of Bi-doped TiO2 and its solar photocatalytic activity for the degradation of isoproturon herbicide, Mater. Res. Bull. 46 (2011) 1766–1771.

[87] M. Baitimirova, R. Viter, J. Andzane, A. van Der Lee, D. Voiry, I. Iatsunskyi, E. Coy, L. Mikoliunaite, S. Tumenas, K. Załęski, Tuning of structural and optical properties of graphene/ZnO nanolaminates, J. Phys. Chem. C 120 (2016) 23716–23725.

[88] J. Wang, J. Huang, H. Xie, A. Qu, Synthesis of g-C3N4/TiO2 with enhanced photocatalytic activity for H2 evolution by a simple method, Int. J. Hydrog. Energy 39 (2014) 6354–6363.

[89] P. Chen, H. Liu, Y. Sun, J. Li, W. Cui, W. Zhang, X. Yuan, Z. Wang, Y. Zhang, F. Dong, Bi metal prevents the deactivation of oxygen vacancies in Bi2O2CO3 for stable and efficient photocatalytic NO abatement, Appl. Catal. B Environ. 264 (2020) 118545.

[90] G. Rajender, J. Kumar, P. Giri, Interfacial charge transfer in oxygen deficient TiO2-graphene quantum dot hybrid and its influence on the enhanced visible light photocatalysis, Appl. Catal. B Environ. 224 (2018) 960–972.

[91] Z. Bian, J. Ren, J. Zhu, S. Wang, Y. Lu, H. Li, Self-assembly of BixTi1− xO2 visible photocatalyst with core–shell structure and enhanced activity, Appl. Catal. B Environ. 89 (2009) 577–582.

[92] W.F. Yao, H. Wang, X.H. Xu, X.F. Cheng, J. Huang, S.X. Shang, X.N. Yang, M. Wang, Photocatalytic property of bismuth titanate Bi12TiO20 crystals, Appl. Catal. A Gen. 243 (2003) 185–190.

[93] Y.-P. Yuan, L.-S. Yin, S.-W. Cao, G.-S. Xu, C.-H. Li, C. Xue, Improving photocatalytic hydrogen production of metal–organic framework UiO-66 octahedrons by dye-sensitization, Appl. Catal. B Environ. 168 (2015) 572–576.

[94] A. Melillo, M. Cabrero-Antonino, S. Navalón, M. Álvaro, B. Ferrer, H. Garcia, Enhancing visible-light photocatalytic activity for overall water splitting in UiO-66 by controlling metal node composition, Appl. Catal. B Environ. 278 (2020) 119345.

[95] X. Peng, L. Ye, Y. Ding, L. Yi, C. Zhang, Z. Wen, Nanohybrid photocatalysts with ZnIn2S4 nanosheets encapsulated UiO-66 octahedral nanoparticles for visible-light-driven hydrogen generation, Appl. Catal. B Environ. 260 (2020) 118152.

[96] Z. Wang, Z. Jin, H. Yuan, G. Wang, B. Ma, Orderly-designed Ni2P nanoparticles on g-C3N4 and UiO-66 for efficient solar water splitting, J. Colloid Interface Sci. 532 (2018) 287–299.

[97] A. Melillo, M. Cabrero-Antonino, B. Ferrer, A. Dhakshinamoorthy, H.G. Baldoví, S. Navalón, MOF-on-MOF composites with UiO-66-based materials as photocatalysts for the overall water splitting under sunlight irradiation, Energy Fuel 37 (2023) 5457–5468.

[98] A.K. Singh, S. Gonuguntla, B. Mahajan, U. Pal, Noble metal-free integrated UiO-66-PANI-co 3 O 4 catalyst for visible-light-induced H 2 production, Chem. Commun. 55 (2019) 14494–14497.

[99] J.-J. Zhou, R. Wang, X.-L. Liu, F.-M. Peng, C.-H. Li, F. Teng, Y.-P. Yuan, In situ growth of CdS nanoparticles on UiO-66 metal-organic framework octahedrons for enhanced photocatalytic hydrogen production under visible light irradiation, Appl. Surf. Sci. 346 (2015) 278–283.

[100] A. Jamma, B. Jaksani, C.S. Vennapoosa, S. Gonuguntla, S. Sk, M. Ahmadipour, I. Mondal, U. Pal, Defect-rich UiO-66@ gC 3 N 4/Ni frameworks as efficient water splitting photocatalysts, Mater. Adv. 5 (2024) 2785–2796.

[101] S. Sudarsono, N.K. Salsabila, R. Asih, G. Yudoyono, D. Darminto, Optical properties of anatase TiO2: Computational and experimental studies, in: AIP Conference Proceedings, AIP Publishing, 2023.

[102] M.S. Devi, S. Abinaya, T. Maiyalagan, G. Keerthiga, Nanorods of α-Bi2O3 for photocatalytic degradation of methylene blue, Mater Today Proc 50 (2022) 2840–2846.

[103] J. Yang, X. Chang, F. Wei, Z. Lv, H. Liu, Z. Li, W. Wu, L. Qian, High performance photocatalyst TiO2@ UiO-66 applied to degradation of methyl orange, Discover Nano 18 (2023) 112.

[104] I. Timrov, Ab initio study of plasmons and electron-phonon coupling in bismuth: from free-carrier absorption towards a new method for electron energy-loss spectroscopy, Ecole Polytech. X (2013).